

Article

Research on the Distributed Propeller Slipstream Effect of UAV Wing Based on the Actuator Disk Method

Mingzhi Cao, Kun Liu, Chunqiang Wang, Jingbo Wei * and Zijie Qin 

School of Aeronautics and Astronautics, Sun Yat-Sen University, Shenzhen 518107, China; caomzh6@mail2.sysu.edu.cn (M.C.)

* Correspondence: weijb5@mail.sysu.edu.cn

Abstract: Distributed electric propulsion technology has great potential and advantages in the development of drones. In this paper, to study the slipstream effect of distributed propellers, the actuator disk method was used to verify a single propeller, and the calculated thrust was in good agreement with the test results. Then, based on the actuator disk method, the influence of different installation positions on the slipstream effect was studied, and the distributed propeller layout was optimized by a genetic algorithm to improve the low-speed performance of the unmanned aerial vehicle (UAV) during the take-off phase and increase the cruise duration. The analysis results showed that the lift of the wing will be larger when the propellers are higher than the wing. The wing lift and drag of the counter-rotating are less than those of the co-rotating. Compared with the original layout, the lift coefficient of the optimized distributed propeller layout is significantly increased by 30.97%, while the lift/drag ratio is increased by 7.34%. Finally, we designed the test platform and qualitatively verified the calculated results without quantitative verification.

Keywords: distributed electric propulsion; wing-propeller interaction; actuator disk method; slipstream



Citation: Cao, M.; Liu, K.; Wang, C.; Wei, J.; Qin, Z. Research on the Distributed Propeller Slipstream Effect of UAV Wing Based on the Actuator Disk Method. *Drones* **2023**, *7*, 566. <https://doi.org/10.3390/drones7090566>

Academic Editor: Diego González-Aguilera

Received: 16 July 2023

Revised: 23 August 2023

Accepted: 25 August 2023

Published: 4 September 2023



Copyright: © 2023 by the authors. Licensee MDPI, Basel, Switzerland. This article is an open access article distributed under the terms and conditions of the Creative Commons Attribution (CC BY) license (<https://creativecommons.org/licenses/by/4.0/>).

1. Introduction

As environmental performance standards for aircraft increase worldwide, largely due to concerns over noise pollution, exhaust emissions, and greenhouse gas contributions, the reliance on oil resources is being challenged. Consequently, electric and distributed propulsion technologies have gained substantial interest in the unmanned aerial vehicle (UAV) sector. Electric aircraft, which use motors to drive propellers and devices such as ducted fans to generate forward thrust, are spearheading the development of future aircraft characterized by low emissions, reduced noise, and high efficiency. Utilizing pure electric or hybrid propeller propulsion technologies can enhance propulsion efficiency while also capitalizing on the propeller's slipstream effect. This allows for an optimal aerodynamic layout, significantly improving the aircraft's flight performance, and catering to both short-range and extended endurance flights [1]. In recent years, the National Aeronautics and Space Administration (NASA) has conducted numerous studies on distributed propeller electric propulsion technology [2–6]. This includes the design of a Hybrid Electric Integrated Systems Testbed (HEIST), the application of Leading Edge Asynchronous Propeller Technology (LEAPTech), and the successful completion of a flight test for the X-57 distributed propeller electric propulsion demonstrator.

Currently, there is a vast array of literature available on distributed propeller electric propulsion technology [7,8]. Patterson et al. [9] evaluated the performance of the X-57 distributed high-lift propeller during the take-off and landing phases. They concluded that distributed high-lift propellers could enhance lift at low speeds by accelerating airflow over the wing and retracting against the nacelle during high-speed flight to minimize drag. Veldhuis et al. [10] analyzed the aerodynamic performance of a single propeller positioned over the wing using numerical methods corroborated with wind tunnel validation. They

identified bilateral aerodynamic coupling between the propeller and the wing. Specifically, a configuration where the propeller was attached to the flap resulted in wing lift increases of 8% and 3% in cruise and high-lift conditions, respectively. Additionally, they utilized wind tunnels to experimentally investigate the aerodynamic interactions of distributed propellers during forward flight [11]. The induced velocities from adjacent propeller slipstreams resulted in local loading variations on the propeller disk, ranging between 5% and 10% of the average disk loading. However, a comprehensive understanding of the propeller installation position's effect on slipstream performance remains elusive. Veldhuis et al. carried out a wind tunnel experiment, varying the propeller position along the spanwise direction of the wing [12]. Their findings suggest that the wing performance improvement was maximized when the propeller was situated close to the wingtip, attributed to the attenuation of the wingtip vortex by the propeller swirl. Nonetheless, this experiment was limited to a single propeller, making the prediction of multiple propellers' spanwise location effect on performance challenging. Lei et al. [13] researched the aerodynamic performance of distributed electric propulsion (DEP) with wing interaction with multiple reference frames (MRF) or slip grid technology. They found that when the angle of attack is greater than 16° the lift-to-drag ratio (L/D) of the DEP system increases significantly. Zhang et al. [14] built a DEP demonstrator with 24 "high-lift" electric ducted fans (EDFs) distributed along the wing's trailing edge to investigate and quantify the aerodynamic-propulsion interaction effect of the wing section. They found that the EDFs can produce significant lift increment and drag reduction simultaneously. Cheng et al. [15] studied the aerodynamic performance of the DEP configuration. The results show that as the propeller number increases, the lift-to-drag ratio decreases, but the wing's lift efficiency increases.

Numerical simulation of propeller slipstream typically employs steady solutions based on the actuator disk method (ADM) [16] and unsteady solutions based on the slip method [17]. A comparative analysis conducted by Stokkermans et al. involving ADM and full computational fluid dynamics (CFD) found that ADM considerably reduced calculation time while preserving high accuracy [18]. Stoll et al. [19] employed the actuator disk model to simulate the preliminary LEAPTech concept aircraft with constant values. Their results demonstrated that the aircraft's lift coefficient could reach 5.2, thereby significantly improving the cruise lift-to-drag ratio. Youngrock et al. [20] scrutinized the aerodynamic performances of a wing and multiple propellers via a parametric analysis of wing-propeller interactions, based on the actuator disk method. Their findings revealed that an increment in the number of propellers increased not only the wing lift and drag, but also the propeller thrust and power. The actuator disk method can considerably reduce calculation time while preserving high accuracy, which is suitable for the study of propeller slipstream.

Optimization is the process of obtaining the greatest or least objective function value for a set of inputs. The optimization algorithm is widely used in electronics, communication, computers, automation, robots, and other fields [21–24]. Propeller layout design may be seen as a multi-objective optimization problem. Chen et al. [25] adopted an efficient optimization algorithm based on a genetic algorithm (GA) and the Kriging agent model to optimize the induced velocity distribution of slip flow and obtain a higher lift/drag ratio. Clarke et al. [26] optimized multi-propeller and multi-rotor aircraft to minimize total energy consumed. Optimized results indicate a 5–10% reduction in battery power consumption.

Existing research primarily centers on the impacts of the number of propellers and their rotation direction on the aerodynamic performance of UAVs during take-off. However, less attention has been given to the relative height between the propeller and the wing, and the horizontal distance between the propeller and the wing's leading edge. The aim of this study is to explore these less concerned areas, specifically the relative height of the propeller to the wing, the distance between the propeller and the wing's leading edge, and the rotation direction of the propeller, building upon the findings of previous research. In order to improve the low-speed performance of the UAV during the take-off phase and increase the cruise duration, the installation position of the propeller is optimized. A genetic algorithm is employed to optimize the wing's maximum lift coefficient and lift/drag ratio

considering three variables: propeller height, forward distance, and spanwise position. This would aid in determining the propeller installation layout. For numerical calculations in this study, the actuator disk model is utilized.

2. Actuator Disk Model

In the process of multi-objective optimization, it is necessary to perform multiple numerical simulations on the distributed propeller slipstream. Utilizing the unsteady slip grid method would generate a considerable volume of calculations, thereby consuming significant computing resources and extending the computation time. To enhance computational efficiency and expedite the optimization process, we substituted the real propeller with the actuator disk. This enabled us to execute a steady-state solution, simulating the distributed propeller slipstream and facilitating rapid optimization.

The actuator disk method [27] simplifies the rotating area of the blade into a disk of negligible thickness. It employs a time-averaged, steady-state approximation to model the airflow entering and exiting the disk. Given identical parameters, including the number of blades, radius, width, hub width, blade installation angle, twist angle, and rotational speed, among others, the acceleration and swirl effect exerted on the airflow by the actuator disk closely mirror those of an actual propeller blade. Upon the propeller’s operation, the associated thrust and torque result from the alterations in air pressure and rotational momentum experienced both upstream and downstream of the actuator disk. At a radius r from the center of the propeller, the thrust force and torque of the differential can be mathematically expressed. The relevant equations are as follows:

$$\begin{aligned} dT &= \frac{1}{2} \rho W^2 (C_l \cos \phi - C_d \sin \phi) c dr \\ dQ &= \frac{r}{2} \rho W^2 (C_l \sin \phi + C_d \cos \phi) c r dr \end{aligned} \tag{1}$$

where C_l , C_d , and c are the lift coefficient, drag coefficient, and chord length of the blade element at r , respectively; ρ , W , and ϕ are the density of the local airflow, the resultant velocity of the relative blade, and the induced angle of attack, respectively. The airflow velocity at a point before the propeller is (\bar{u}, v_θ, v_r) , and ω is the rotational angular velocity of the propeller. The cylindrical coordinate system is used here to describe the airflow velocity. \bar{u} represents radial velocity, v_θ represents tangential velocity, and v_r represents normal velocity. Then, the resultant velocity is:

$$W = \sqrt{\bar{u}^2 + (\omega r - v_\theta)^2} \tag{2}$$

and the induced angle of attack is:

$$\phi = \arctan\left(\frac{\bar{u}}{\omega r - v_\theta}\right) \tag{3}$$

When the actuator disk model is used to solve the calculation, ρ , \bar{u} , and v_r remain unchanged both upstream and downstream of the disk. In this paper, we designate the front of the actuator disk as the outflow boundary, and the rear as the inflow boundary. Simultaneously, we establish parameters, including the number of blades, radius, width, hub width, blade installation angle, twist angle, and rotational speed, among others. Then, we read the lift/drag coefficient of the propeller blade at different angles of attack.

To verify the accuracy of the numerical calculation of the actuator disk model, the calculation is compared with the test data for a propeller. The propeller test data are mentioned in the literature [28], and the detailed blade parameters are given in Table 1. The propeller is a two-bladed blade with a tip radius of 0.381 m, while the hub radius has a tip radius of 0.2, and the blade profile is a Clark Y airfoil. Two cases were selected for verification. The velocity of the inflow in the experiment is 30 m/s. Rotation speed

is 2420 r/min for case 1 and 3200 r/min for case 2. The comparison between the results calculated by the actuator disk model and the test data can be seen in Table 2.

Table 1. Blade parameters of Clark Y airfoil twin-bladed blades [28].

Relative Radius	Local Blade Angle	c/R	Relative Thickness
0.2	39.88°	0.107	0.350
0.3	30.70°	0.144	0.274
0.4	26.60°	0.169	0.204
0.5	23.00°	0.178	0.171
0.6	19.80°	0.172	0.154
0.7	17.00°	0.159	0.146
0.8	14.65°	0.139	0.140
0.9	13.00°	0.117	0.135
1.0	12.00°	0.092	0.130

Table 2. The calculation results of propeller thrust are compared with the test data.

Case	Experimental Values C_T	Calculated Value C_T	Relative Error, %
1	0.0655	0.0639	2.43
2	0.0560	0.0538	3.93

As seen from Table 2, the actuator disk model is adopted in this paper to conduct a numerical simulation of the propeller, and the deviations between the calculated thrust value and the test value are less than 4%, which means the accuracy of the actuator disk model.

Figure 1 presents the pressure cloud diagram, illustrating the conditions both upstream and downstream of the actuator disk. The pressure in the upstream region of the disk diminishes due to the contraction engendered by propeller rotation. Conversely, there is a substantial pressure increment in the downstream area of the disk. The pressure in front and behind the disk of the propeller is discontinuous, which conforms to the rationality of momentum theory. The pressure behind the disk is greater than the pressure in front of the disk, resulting in forward thrust.

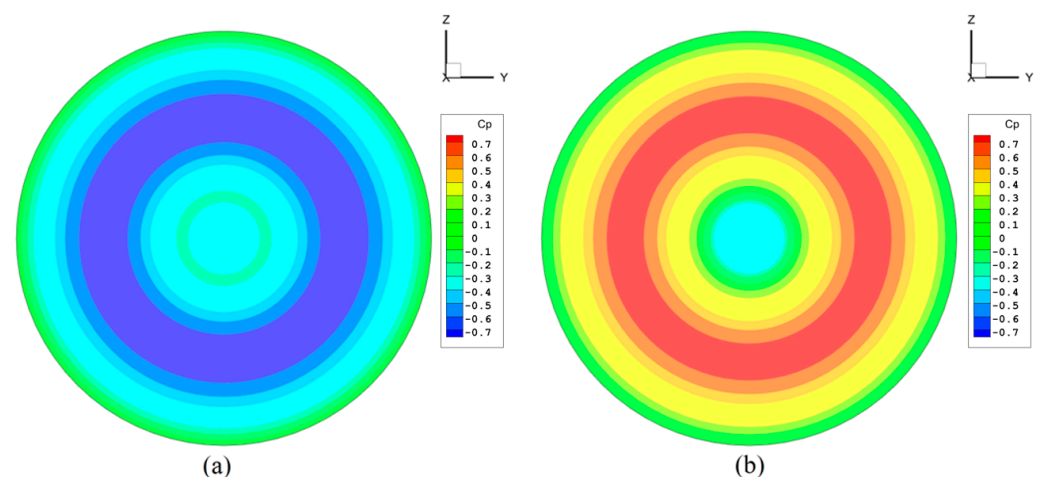


Figure 1. Pressure cloud diagram: (a) before disk; (b) after disk.

Figure 2 presents the velocity vector diagram, illustrating the conditions both upstream and downstream of the actuator disk. Figure 2 is the velocity vector diagram before and after the actuator disk. The flow in front of the disk is found to have no circumferential velocity. In contrast, the downstream flow manifests a discernible circumferential velocity,

indicating the presence of a swirl flow. This pattern aligns with the actual aerodynamic behavior, verifying the model's validity.

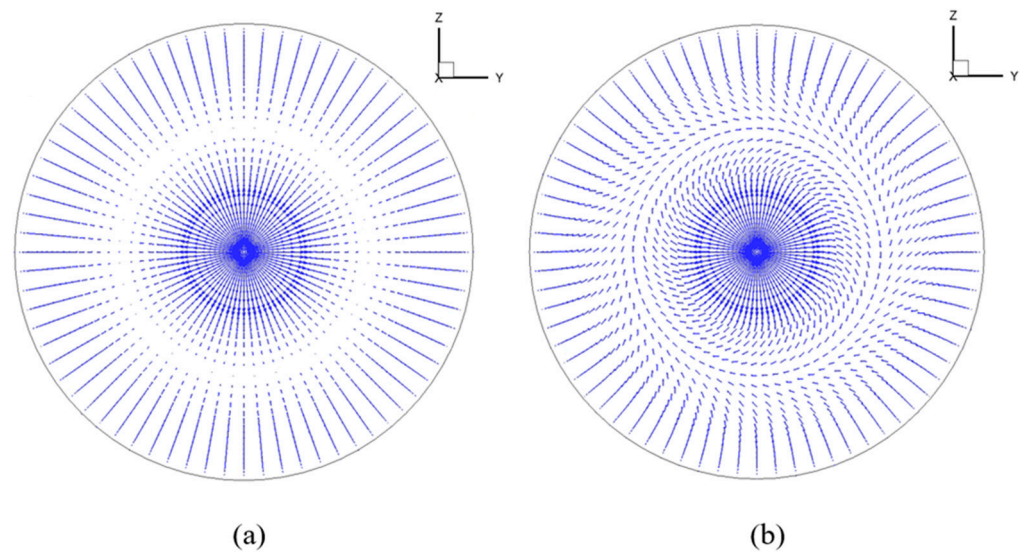


Figure 2. Velocity vector diagram: (a) before disk; (b) after disk.

The actuator disk method employed in this paper replicates the real aerodynamic effects of propellers. This makes it a valuable tool for fulfilling the numerical simulation needs of future optimization designs for distributed propeller layouts.

3. Analysis of Factors Affecting Slipstream Characteristics

Considering that the axial-induced velocity at the rear of the propeller disk is different in different radial positions, the height of the propeller relative to the wing has an influence on the slipstream effect. According to classical momentum theory, the axial velocity of the wake after the propeller disk is a continuous acceleration process, so the distance between the propeller and the leading edge of the wing will affect the axial-induced velocity when the slipstream reaches the wing [29]. Consequently, we used the actuator disk method to preliminarily analyze the influence of relative height and distance from the leading edge of the wing on the slipstream characteristics of the propeller.

3.1. Introduction of the Propeller + Wing Model

The test object is a combined model of a flat wing and four propellers. The analysis was performed for the semi-span with the propeller, because the shape is symmetric. The UAV wing employs the NACA2412 airfoil with a semi-span of 2 m and a chord of 0.5 m, and the four propellers are two-blade propellers with Clark Y airfoil. The propellers have a diameter of 0.4 m. The actuator disk model is adopted, and the four propellers are represented by the disk without thickness. The propellers are perpendicular to the chord line of the wing, which means the propellers will have the same angle of attack as the wing. Taking the wing root as the starting point, the distribution distances of the four disk centers along the wing spanwise are 0.25 m, 0.75 m, 1.25 m, and 1.75 m. The specific 3D model can be seen in Figure 3a, and the inflow direction is the X-axis direction. Figure 3b illustrates the velocity vector of the slipstream. In this context, " v_∞ " corresponds to the free incoming velocity, " v_p " represents the axial-induced velocity after the propeller, and " v_{ep} " denotes the effective velocity of the slipstream.

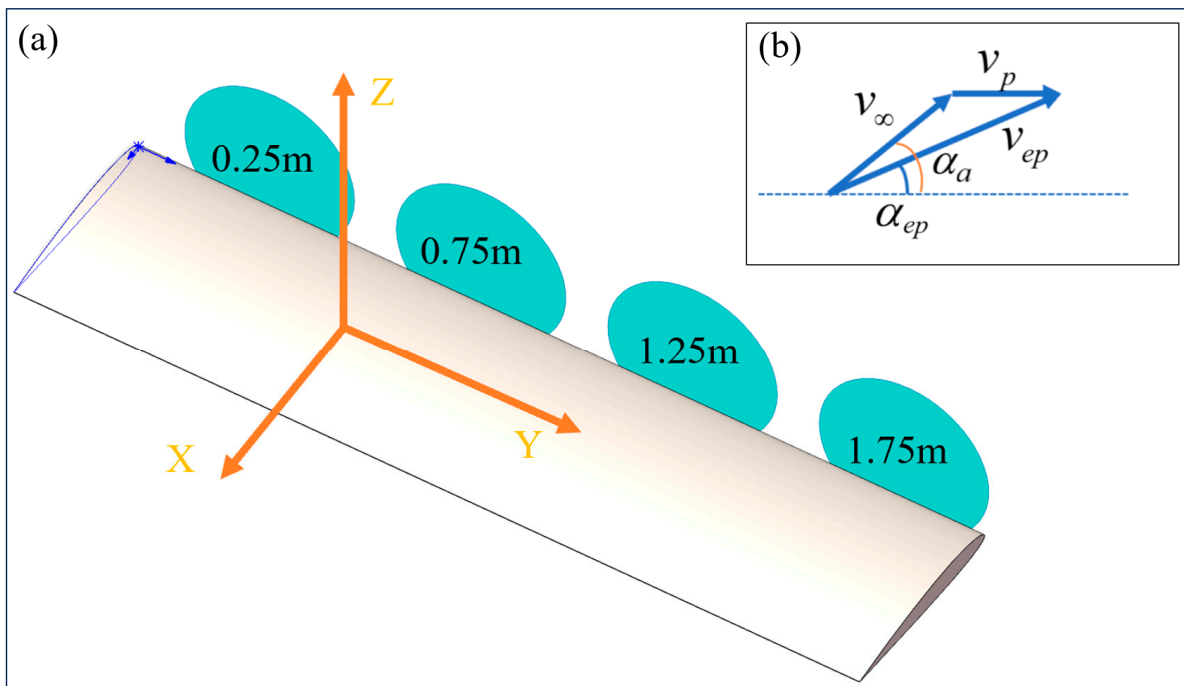


Figure 3. Geometric model of propeller + wing. (a) The specific 3D model; (b) the velocity vector of the slipstream.

In this paper, computational fluid dynamics (CFD) calculations are performed based on the Reynolds-averaged Navier–Stokes (RANS) equations. The turbulence model used is grounded in the two-equation shear stress transport (SST) model. Figure 4 shows the unstructured grid of this model. Table 3 shows that the number of grids has little effect on the calculation results, and the details of the grid can be found in Table 4.

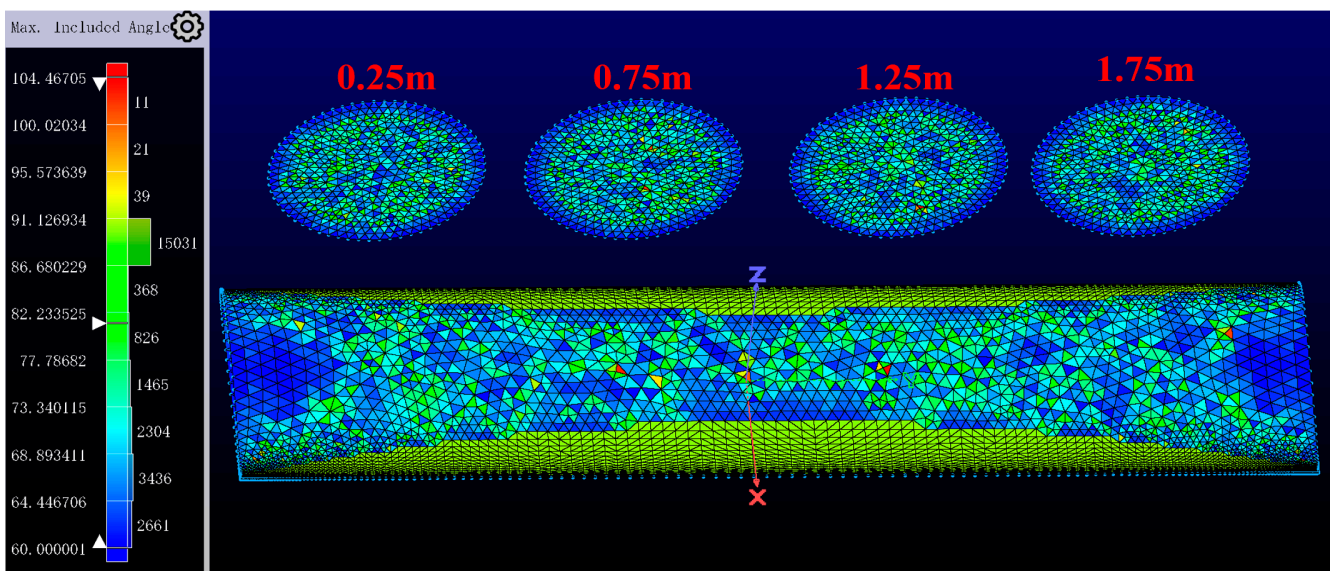


Figure 4. Unstructured grid.

Table 3. Grid independence verification.

Number of Grids	Cl	Cd
1 million	0.8872	0.06092
1.5 million	0.8896	0.06111
2 million	0.8929	0.06188

Table 4. Specific grid information.

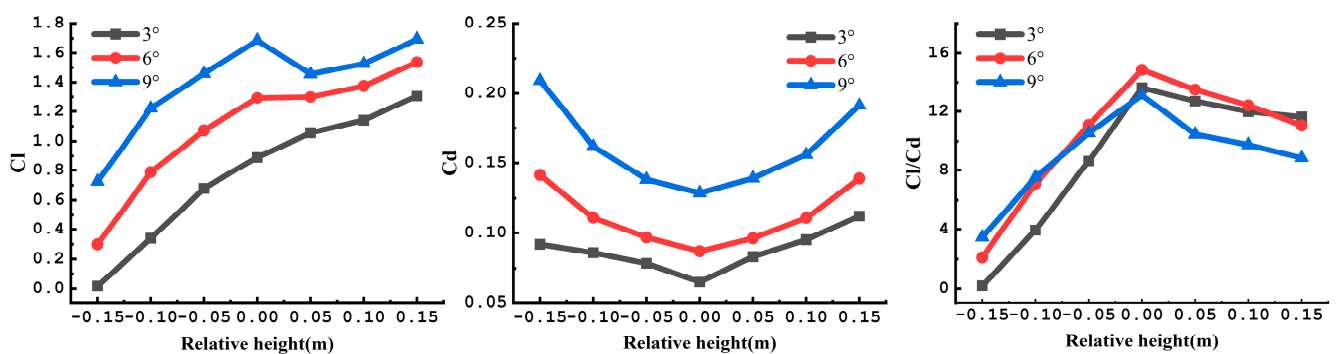
Attribute	Setup
Grid type	Tetrahedral unstructured mesh
Minimum mesh size	0.65 mm
Grid number	1,472,398
Y+	1.0

The direction of incoming flow aligns with the X-axis, which corresponds to the wing's chord direction. The Y-axis is the spanwise direction, and the Z-axis is perpendicular to the plane where the chord and spanwise direction of the wing are located, satisfying the right-hand rule. The simulation test conditions are as follows: the incoming flow speed is 20 m/s; the rotation rate of the four propellers is 2800 r/min; and the steering is clockwise rotation (viewed along the negative X-axis).

3.2. Relative Height of Propeller

Initially, we define the position as zero when the center of the propeller disk aligns with the chord line of the wing. This implies that the relative height of the propeller to the wing is zero. If the propeller is positioned higher than the wing, we assign a positive direction; conversely, a negative direction is used when the propeller is lower than the wing. For these simulations, the propeller's diameter is set at 0.4 m. The propellers are positioned 0.1 m forward of the wing.

Figure 5 illustrates the interrelationships between the lift coefficient, drag coefficient, and lift/drag ratio of a UAV wing at angles of attack of 3° , 6° , and 9° , in relation to the relative height of the propellers. It is observed that the lift coefficient of the wing positively correlates with the increasing relative height of the propellers. Furthermore, as the propeller moves farther from the wing, an approximate increase in the drag coefficient is noticed, with the drag coefficient reaching its lowest value when the relative height of the propellers from the wing is zero. As a result, the lift/drag ratio diminishes as the propeller descends below the wing and reaches its maximum when the relative height of the propeller from the wing is zero.

**Figure 5.** Curves of the lift coefficient, drag coefficient, lift/drag ratio, and relative height at different angles of attack.

These observations are further validated by Figure 6, which portrays the distribution of the upper surface pressure coefficient of the wing. In the legend, "RH" is an abbreviation

for the relative height of the propeller. When the propeller is positioned at a relative height of -0.1 m, fewer low-pressure areas are observed on the upper surface of the wing. However, as the relative height of the propellers increases, more low-pressure areas become evident on the wing's upper surface, indicating an increase in lift obtained by the wing.

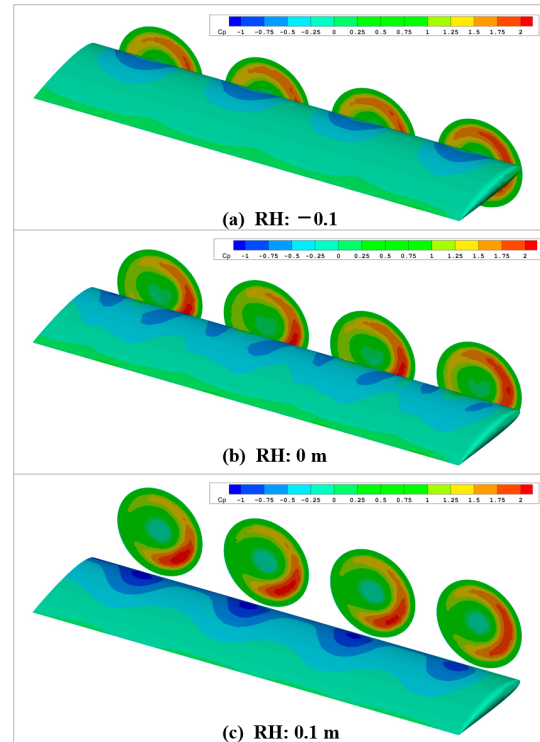


Figure 6. Pressure coefficient distribution at different relative heights of propellers.

Further, we can analyze the sectional pressure coefficient along the wing chordwise. At an angle of attack of 6° , the chordal surface at 1.25 m (which corresponds to the center of the third propeller disk) in the y -direction of the wing is selected to extract the pressure coefficient data. This data is depicted in Figure 7. As the figure shows, when the relative height is -0.1 m (indicating the propeller is positioned under the wing), the pressure coefficient on the lower surface of the leading edge of the wing is smaller than the pressure coefficient on the top surface. As a whole, the pressure difference between the upper and lower surfaces of the wing is the smallest. When the relative height is positive, the pressure difference between the upper and lower surfaces of the wing is larger, and the wing can obtain greater lift. When designing a distributed propeller layout, the propeller can be properly mounted at a certain height above the wing.

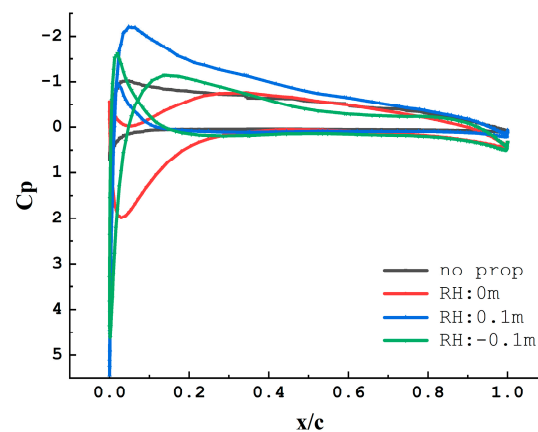


Figure 7. Sectional pressure coefficient of the wing with different relative heights ($y = 1.25$ m).

3.3. Distance between the Propeller and Wing Leading Edge

According to the momentum theory, when the propeller is far away from the leading edge of the wing, the incoming airstream preceding the propellers will accelerate fully, thereby enhancing the slipstream effect. Figure 8 shows the lift coefficient, drag coefficient, and lift/drag ratio of the UAV wing at angles of attack of 3°, 6°, and 9°, plotted against the distance between the propeller and the wing’s leading edge. The diameter of the propeller is maintained at 0.4 m, and the relative height is 0 m. The lift coefficient of the wing increases slightly with increasing distance between the propeller and the wing leading edge, while the drag coefficient of the wing decreases with increasing distance between the propeller and the wing leading edge. Collectively, the lift/drag ratio of the wing increases with increasing leading-edge distance. According to the momentum theory, the airflow behind the disk has an acceleration. As the propeller distance from the wing’s leading edge increases, the velocity of the air reaching the wing surface also increases, thereby generating additional lift. When the airflow traverses the leading edge of the wing, the velocity decreases on the wing’s leading edge, leading to the formation of a substantial positive pressure area on the wing’s lower surface. Following this, the flow accelerates along the wing surface. Figure 9 illustrates that as the propeller moves further away from the wing’s leading edge, the positive pressure zone at the leading edge of the wing’s lower surface decays more rapidly in the chord direction. This indicates greater airflow acceleration over the lower surface of the leading edge, thereby reducing the drag on the wing.

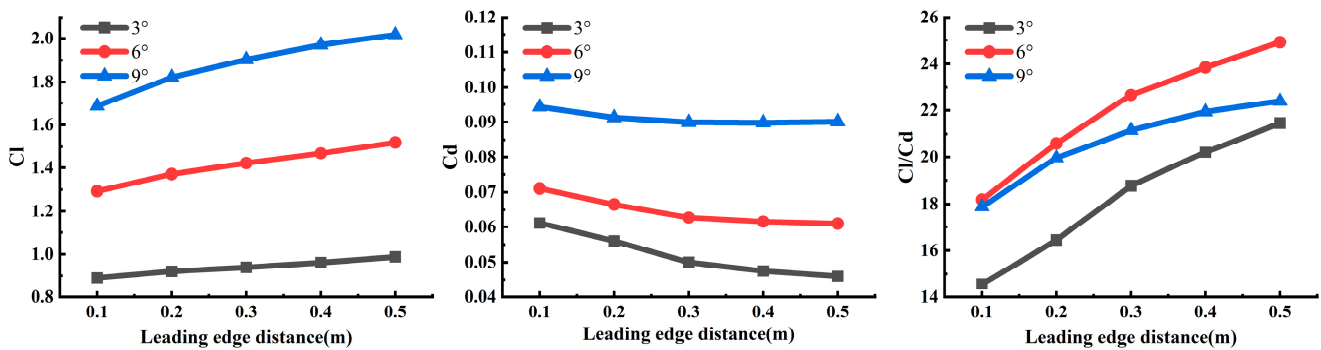


Figure 8. Curves of the lift coefficient, drag coefficient, lift/drag ratio, and leading-edge distance at different angles of attack.

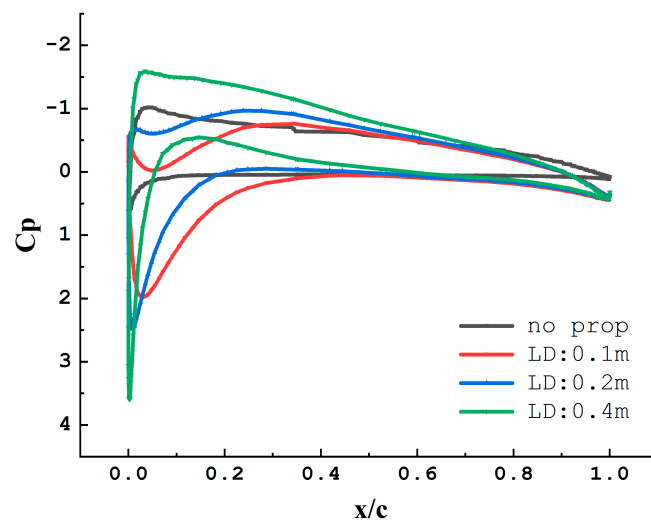


Figure 9. Sectional pressure coefficient of the wing with different leading-edge distances ($y = 1.25$ m).

When the angle of attack is 6° , the chordal surface at 1.25 m (center of the third propeller disk) in the y-direction of the wing is intercepted, and the pressure coefficient data is extracted and drawn, as shown in Figure 9. In the legend, “LD” stands for distance between the propeller and wing leading edge. As the distance between the propeller and the wing’s leading edge progressively expands, a little increase is noted in the wake velocity following the propeller disk. This uptick in wake velocity moderately enhances the airflow velocity on both the upper and lower surfaces of the wing, resulting in decreased pressure. Simultaneously, the location of the minimum pressure point on both the upper and lower surfaces of the wing appears to shift forward.

3.4. Rotating Direction

In order to compare the effect of rotation direction, two cases are designed, as shown in Figure 10. One case is that the four propellers are rotating clockwise (viewed along the negative X-axis). The other case is that the first and third propellers remain unchanged clockwise rotation, and the second and fourth propellers become counterclockwise rotation (2C2A). The impact of the rotating direction on the wing performance is shown in Table 5. The wing lift and drag of the counter-rotating are less than those of the co-rotating for all cases.

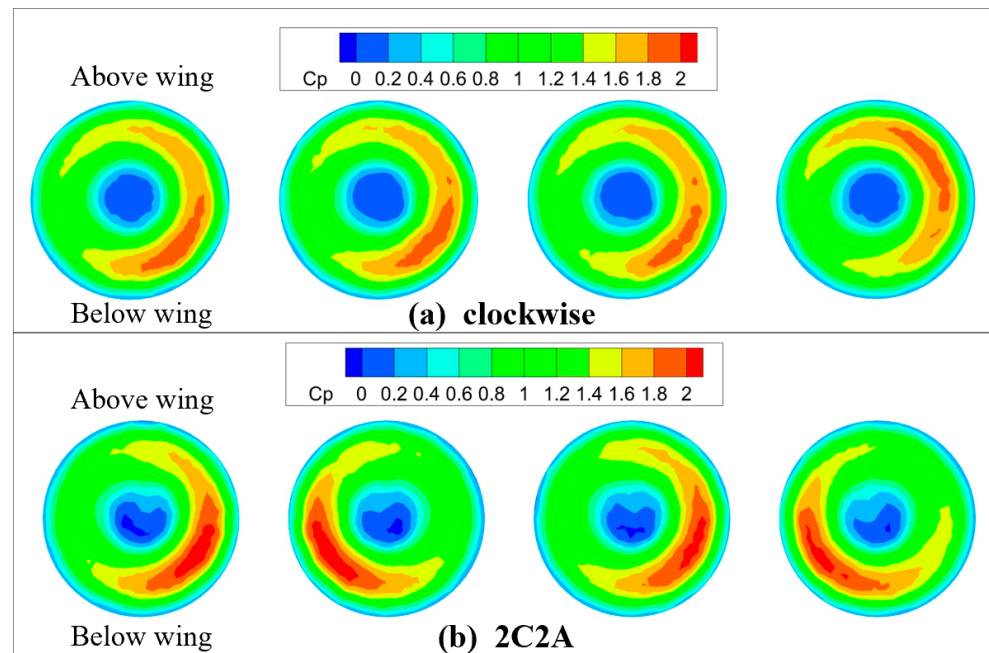


Figure 10. Two cases of propeller rotating direction.

Table 5. Wing performance of the different cases on rotating direction.

Angle of Attack/ $^\circ$	Case	Direction of Rotation	Cl	Cd
3	RH: -0.1 m	clockwise	0.3391049	0.0860269
		2C2A	0.30233191	0.082231
	RH: 0 m	clockwise	0.88957623	0.061112
		2C2A	0.84635478	0.061083
	RH: 0.1 m	clockwise	1.1407378	0.090186
		2C2A	1.1460909	0.095574
	LD: 0.1 m	clockwise	0.88957623	0.061112
		2C2A	0.84635478	0.061083
	LD: 0.4 m	clockwise	0.96076316	0.04753
		2C2A	0.89923285	0.047207

Table 5. Cont.

Angle of Attack/ $^{\circ}$	Case	Direction of Rotation	Cl	Cd
6	RH: -0.1 m	clockwise	0.7882753	0.108963
		2C2A	0.75482708	0.105429
	RH: 0 m	clockwise	1.2923487	0.071081
		2C2A	1.2427707	0.071087
	RH: 0.1 m	clockwise	1.375486	0.098888
	LD: 0.1 m	2C2A	1.3825217	0.106183
clockwise		1.2923487	0.071081	
LD: 0.4 m	2C2A	1.2427707	0.071087	
	clockwise	1.468224	0.080024	
9	RH: -0.1 m	clockwise	1.2209848	0.142
		2C2A	1.1773036	0.13772
	RH: 0 m	clockwise	1.6863144	0.085733
		2C2A	1.629571	0.085745
	RH: 0.1 m	clockwise	1.5740664	0.126201
	LD: 0.1 m	2C2A	1.5249141	0.132127
clockwise		1.6863144	0.085733	
LD: 0.4 m	2C2A	1.629571	0.085745	
	clockwise	1.9705575	0.089835	
		2C2A	1.9157836	0.089122

Figure 11 shows the sectional pressure coefficients along the wing chordwise. In comparison with the lift of the isolated wing, the increment in the lift of the counter-rotating is less than that in the lift of the co-rotating. Because the downwash and upwash generated by the propeller swirl overlap in the wing regions between adjacent propellers.

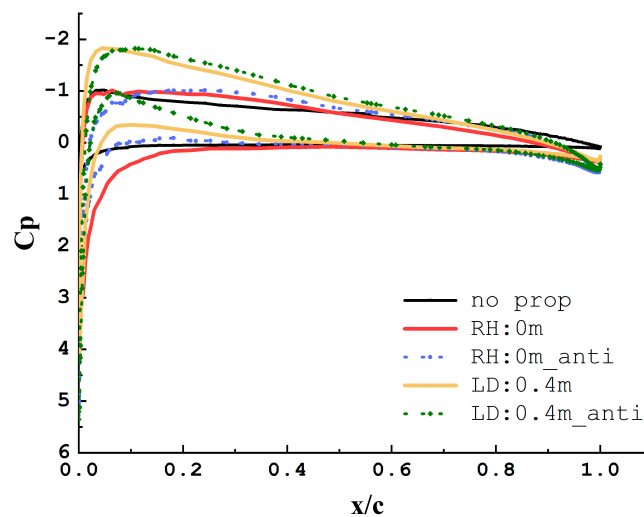


Figure 11. Sectional pressure coefficient of the wing with different rotation direction ($y = 0.65$ m).

4. Genetic Algorithm Optimization

Distributed electric propulsion can make full use of the propeller slipstream to improve the lift of the UAV, improve the low-speed performance of the UAV, increase the wing load, or reduce the take-off distance. It is very important to make good use of the slipstream effect of the propellers to maximize the lift coefficient of the UAV when taking off. However, the low-speed take-off phase is very short compared to the cruise phase, and the UAV pays more attention to the lift/drag ratio during cruise. Therefore, in the process of considering the optimization of distributed propeller installation position, this paper not only cares about the maximum lift coefficient of the UAV, but also pursues to improve the

lift/drag ratio of the UAV. This is a multi-objective optimization problem. In this paper, a multi-objective genetic algorithm is used to achieve the optimization.

4.1. Optimization Introduction

The nondominated sorting genetic algorithm (NSGA) is a multi-objective algorithm based on a genetic algorithm. The primary distinction between the NSGA and the fundamental genetic algorithm lies in NSGA's approach of executing rapid nondominated ranking on individuals prior to the selection operation. This strategy enhances the likelihood of retaining high-performing individuals. Other operations such as selection, crossover, and mutation are identical to those employed in the standard genetic algorithm. Extensive research and testing by numerous scholars have demonstrated that the NSGA surpasses traditional multi-objective genetic algorithms in performance. However, the NSGA is found to still have some shortcomings in practical applications, and the NSGA-II [30–32] has made some improvements to make up for the defects of the NSGA. NSGA-II has three new innovations—a fast nondominated sorting procedure, a fast crowded distance estimation procedure, and a simple crowded comparison operator [32]. NSGA-II has the properties of a fast nondominated sorting procedure, an elitist strategy, a parameter-free approach, and a simple yet efficient constraint-handling method. The NSGA-II procedure is shown in Figure 12.

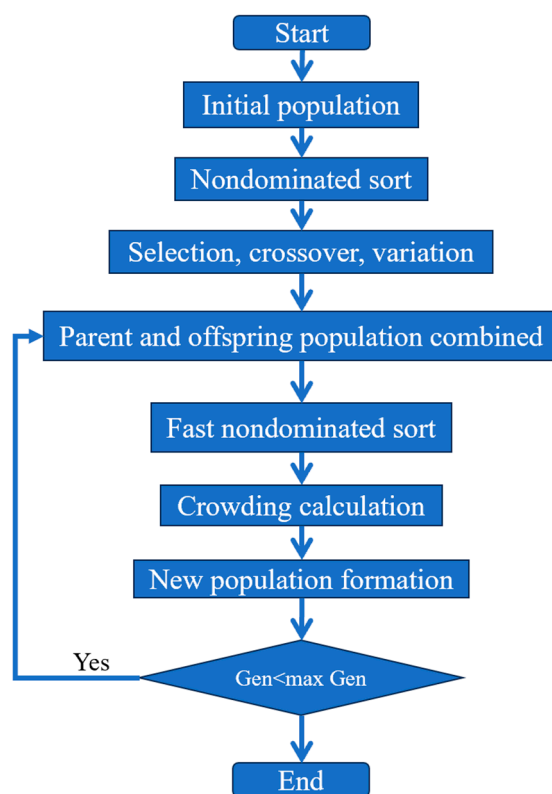


Figure 12. NSGA-II procedure.

Because NSGA-II can optimize multiple targets and find the optimal solution, it is suitable for the optimization of propeller slipstream. We have examined the impact of the distributed propeller slipstream on the semi-span wing, as illustrated in the distributed layout optimization design system diagram (Figure 13). Utilizing techniques such as parametric modeling, T-Rex unstructured meshing, the actuator disk model, and stationary flow numerical simulation methods, we rapidly simulated the flow field of the ‘propeller + wing’ combination and obtained the corresponding aerodynamic data. By implementing the NSGA-II algorithm, we were able to find the global optimal solution.

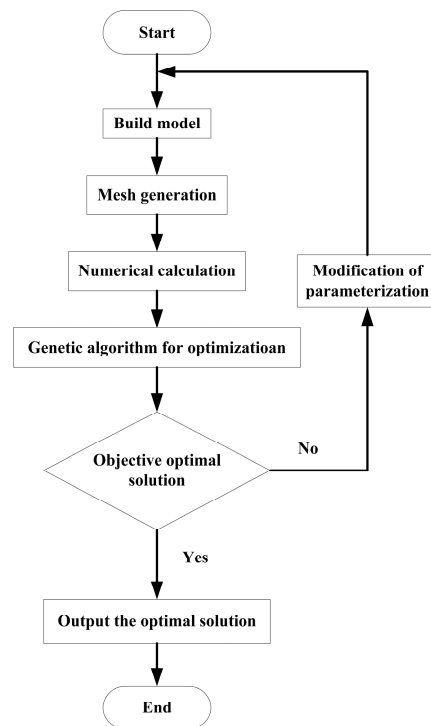


Figure 13. Optimal design system diagram of the distributed propeller aerodynamic layout.

4.2. Analysis of Optimization Results

Distributed propellers improve lift mainly by increasing dynamic pressure on the wing surface through slipstream. The aforementioned “propeller + wing” model is used as the optimization object, as shown in Figure 14. In Figure 14, “x” represents the horizontal distance from the propeller to the leading edge of the wing, and “z” represents the relative height of the propeller to the wing. “y1”, “y2”, “y3”, and “y4”, respectively, represent the spanwise distance from the disk center of the four propeller disks to the wing root. The take-off speed is designed to be 20 m/s, and the angle of attack of the incoming stream is 3° .

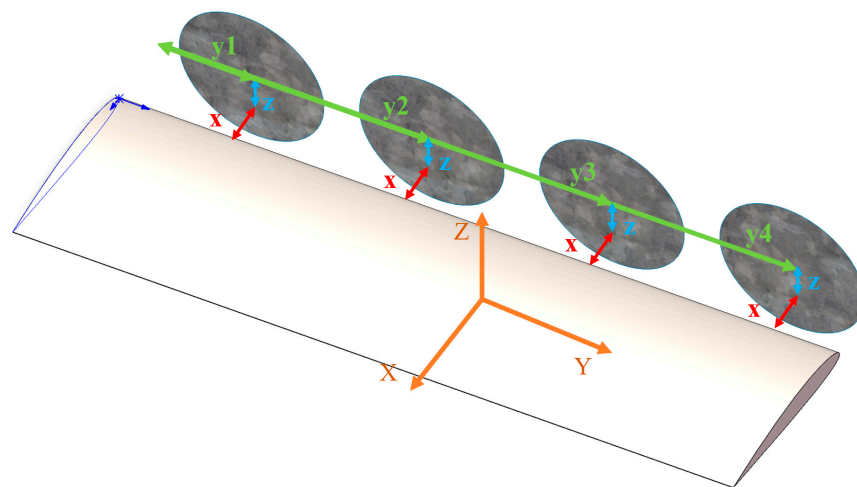


Figure 14. The initial model before optimization.

Considering the influence of the distributed propeller slipstream on the wing during take-off, the dynamic position layout of the distributed propeller aircraft was optimized. The actuator disk model is employed as a substitute for the actual propeller, with the propeller rotation being clockwise (viewed along the -x-direction). Combined with the

above research, the relative height, leading-edge distance, and propeller position in the y-direction are designed as optimization variables, and the optimization objective is to find the maximum lift coefficient and lift/drag ratio of the wing. The constraint conditions are:

$$\begin{aligned} &\text{Objective function : } \min(-C_l/C_d), \min(-C_l) \\ &\text{s.t. } \begin{cases} 0 \leq z \leq 0.2 \\ 0.01 \leq x \leq 0.5 \\ 0.01 \leq y_{i+1} - y_i \leq 0.6, i = 1, 2, 3 \\ y_1 > 0.2 \\ y_4 \leq 2 \end{cases} \end{aligned}$$

The propeller’s radius is set at 0.2 m. Correspondingly, the relative height (“z”) is constrained so as not to exceed this propeller radius. Given that the wing chord length is defined at 0.5 m, the leading-edge distance (“x”) is also constrained to not exceed the wing chord length. The distance between the center of the first propeller disk (“y1”) and the wing root should be greater than the propeller radius, while the center of the fourth propeller disk (“y4”) can extend to the wing tip’s farthest point.

According to the established optimization design system, the installation position of the distributed propeller during take-off is optimized. The NSGA-II algorithm is used for optimization calculation, with the primary generation population set at 12 and the iteration count fixed at 6. The details of the NSGA-II algorithm can be seen in Table 6.

Table 6. The details of the NSGA-II algorithm.

	Parameter
Design variables (input of algorithm)	Relative height (“z”); Leading-edge distance (“x”); Propeller position in the y-direction (“y1”, “y2”, “y3”, “y4”)
Optimization objective (output of algorithm)	Lift coefficient; lift/drag ratio
Population size	12
Number of generations	6

The optimized configuration of the distributed propeller-wing arrangement is depicted in Figure 15. After optimization, the relative height of the propeller is higher than the relative height before optimization, and the leading-edge distance also exhibits an increase. At the same time, the fourth propeller is positioned closer to the wing tip. Refer to Table 7 for details.

Table 7. Propeller variable values before and after optimization.

	x (m)	z (m)	y1 (m)	y2 (m)	y3 (m)	y4 (m)
Before optimization	0.1	0	0.25	0.75	1.25	1.75
Optimized	0.372	0.156	0.262	0.787	1.313	1.839

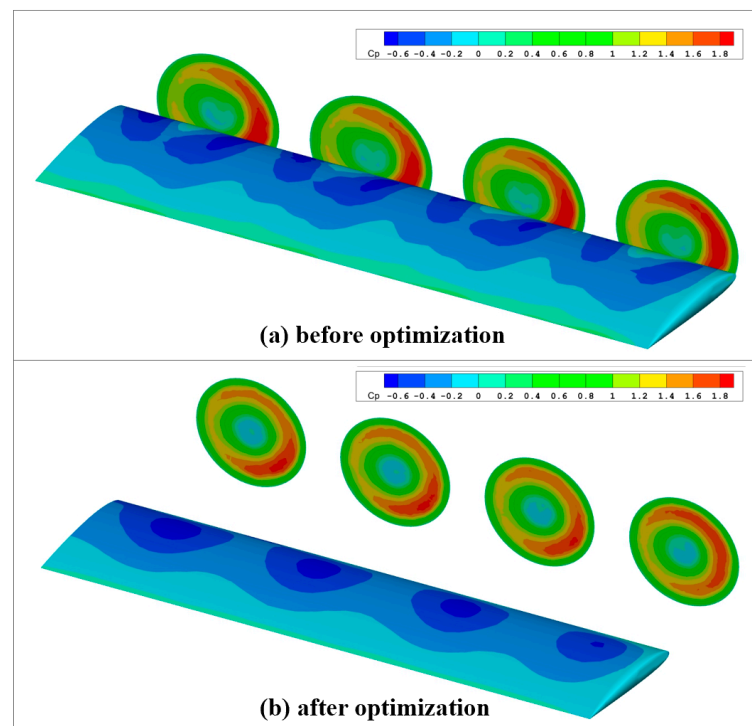


Figure 15. Distributed propeller/wing configuration before and after optimization.

The comparison of the flow field calculation results before and after the optimization of the propeller installation position is instructive. Cloud images of the pressure coefficient on the wing's upper surface for the two layout configurations correspond to Figure 15a,b, respectively. Notably, the slipstream to some degree affects the entire spanwise direction of the wing's leading edge due to the wing's 3D effect. Furthermore, the distributed propeller slipstream significantly influences most areas between the leading edge and $2c/3$ of the wing, where the negative pressure enhancement is relatively obvious. However, the effect on the area between $2c/3$ and the trailing edge is relatively weak, with less obvious negative pressure enhancement. Before optimization, the wing experienced the downwash and upwash effects of the wake flow in the upper half plane of the propeller. The upwash area amplified the local angle of attack of the wing surface, resulting in a larger negative pressure. In contrast, the downwash area decreased the local angle of attack of the wing surface, with a slightly weaker negative pressure compared to the upwash area. The axial-induced velocity behind the propeller disk varies along the propeller's radial direction, resulting in two low-pressure areas on the upper surface of the wing behind the propeller disk, as depicted in Figure 15a. After optimization, with the propeller positioned above the wing, the upwash and downwash effects behind the disk are enhanced. This enhancement significantly amplifies the negative pressure effect of the slipstream on the wing's upper surface, leading to a sizable area of negative pressure enhancement on the wing's upper surface.

From an aerodynamic standpoint, as indicated in Table 8, the optimized wing demonstrates significant improvements. Following the optimization process, the wing's lift coefficient experiences a substantial increase of 30.97%, while the lift/drag ratio improves by 7.34%. These enhancements enhance the UAV's low-speed performance during take-off and extend its cruising time during the cruise phase. Figure 16 illustrates that the axial velocity at the rear of the disk reaches approximately 70 m/s. The alteration in the propeller's relative height amplifies the pressure disparity between the wing's upper and lower surfaces, resulting in a larger lift coefficient. Although this also leads to increased drag, positioning the propellers closer to the wing tip mitigates the formation of tip vortices, thereby augmenting the wing's lift/drag ratio.

Table 8. Comparison of aerodynamic characteristics of wings before and after optimization.

	C_l	C_d	C_l/C_d
The initial	0.88958	0.06531	13.62089
The optimized	1.165133	0.07969	14.62119
Difference	30.97%	22.02%	7.34%

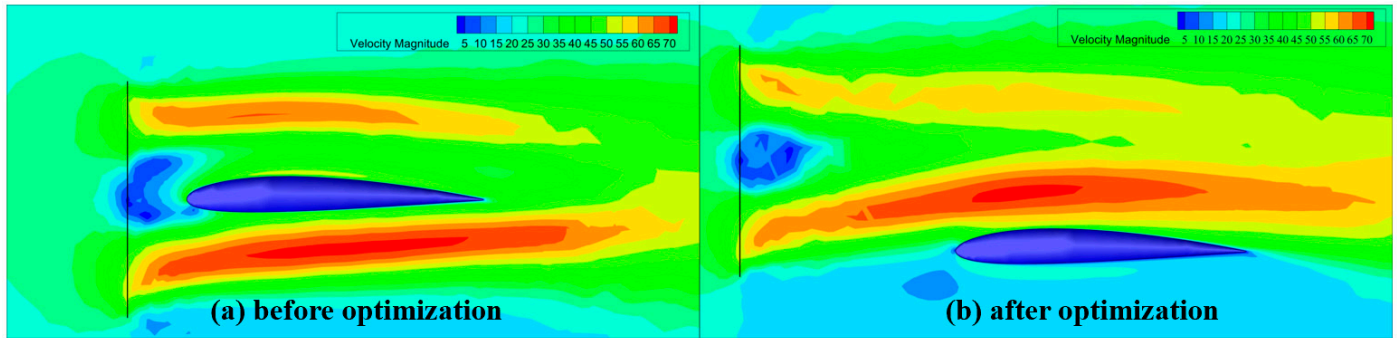


Figure 16. Axial velocity distribution at the rear of the disk (lateral view).

Figure 17 presents a comparison of spanwise pressure coefficients at a quarter-chord position of the wing, both before and after the optimization of the distributed propeller layout. Here, “b” on the X-axis denotes the wing span. Before optimization, eight negative pressure peaks are observed on the upper surface of the wing, with a corresponding number of positive peaks on the lower surface. The area around 0.6–0.7 r, on both sides of each propeller, exhibits the maximum negative pressure. This observation suggests that the axial-induced velocity at the propeller disk’s rear alters with the radial direction. It is at its largest in the 0.6–0.7 r range, while the velocity on either side is considerably smaller. After optimization, the upper surface of the wing displays four negative pressure peaks, whereas the lower surface shows no negative pressure peaks. There is an increase in the upper surface’s negative pressure along the spanwise direction. This implies that the slipstream impacts the entire wing’s spanwise direction. As the propeller’s relative height increases, the primary area through which the propeller disk’s slipstream passes moves to the wing’s upper surface, accelerating the airflow in that region and creating a larger negative pressure area. The slipstream’s effect on the wing’s lower surface is minimal, resulting in no significant change in its pressure coefficient.

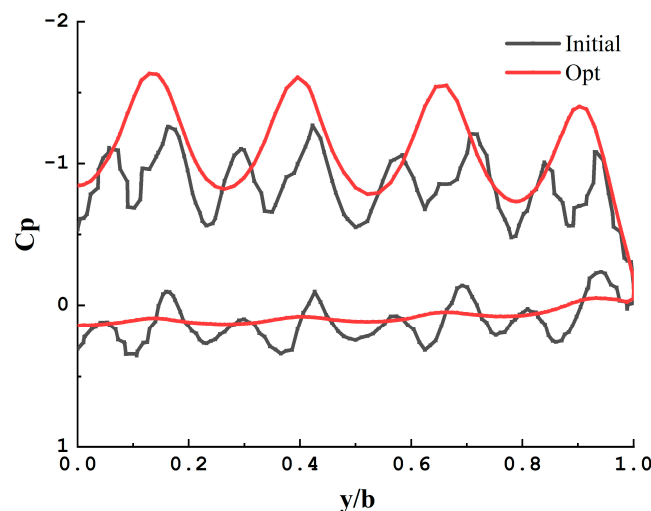


Figure 17. Comparison of the pressure coefficient distribution at the quarter-chord length of the wing before and after optimization.

5. Experimental Verification

This paper details the design of a simple distributed propeller slipstream experimental platform, depicted in Figure 18, intended for slipstream testing. Figure 18a provides a physical layout of the test platform, while Figure 18b illustrates a side view of the same. The platform comprises several components, and details can be found in Table 9.

Table 9. Details of the experimental platform.

Region	Components	Attributes and Functions
a	Eight 10-inch diameter propellers	Provide flow to simulate the test
b	Honeycomb plate	7.5 mm aperture, retain the axial-induced speed of the front propellers, isolate the tangential induced speed, and provide uniform incoming flow
c	“Propeller + wing” model	/
d	Rotation area	Change the wing mounting angle
e	Sliding area	Change the height and the horizontal distance of the wing

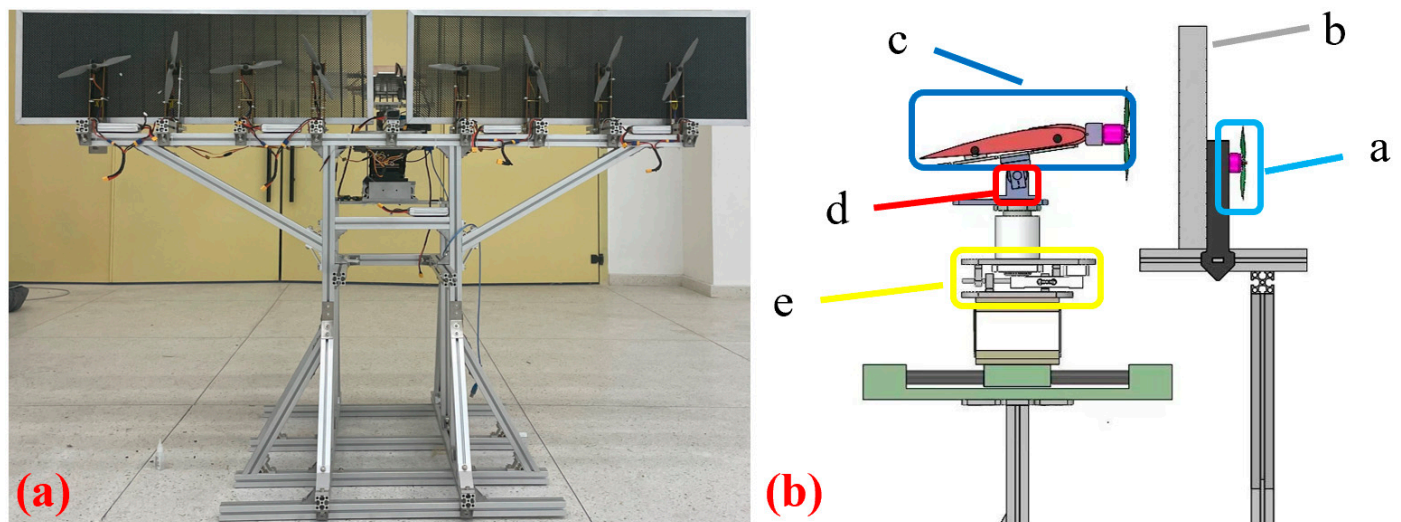


Figure 18. (a) Distributed propeller slipstream experimental platform; (b) a side view of the experimental platform.

The platform utilizes a combination of a front “propeller + honeycomb panel” to generate uniform airflow. Adjustable rotation and sliding areas facilitate modifications to the wing’s height and horizontal distance. A pressure sensor is positioned at the center of the platform to measure the pressure exerted on it by the weight of the entire wing situated above the sensor. Pressure sensors capture varying pressure data of the wing, whether the leading-edge propellers are in operation or not. The lift generated by the wing can be determined by calculating the pressure difference. For this experiment, a wing model with a wingspan of 2 m and a chord length of 0.3 m is employed. Six 10-inch diameter propellers are affixed to the wing’s leading edge. Throughout the test, the speed of the propellers remains constant. A simulated uniform incoming flow with an approximate velocity of 20 m/s was employed. While the experimental results cannot be directly compared with the simulation data, they still hold comparative value.

To examine the effects of relative height and leading-edge distance on slipstream influence, a series of corresponding experiments are conducted. These tests incorporate variations in the wing mounting angle, specifically at 1° , 3° , and 5° , and assess the impact of different relative heights and forward distances of the propellers. The experimental results, depicted in Figure 19, reveal that wing lift tends to escalate with an increase in relative height. Conversely, an increase in the leading-edge distance results in a reduction in lift force. This effect can be attributed to the velocity of the air behind the disk slowing down,

due to the presence of the surrounding stationary air, before it reaches the downstream wing surface.

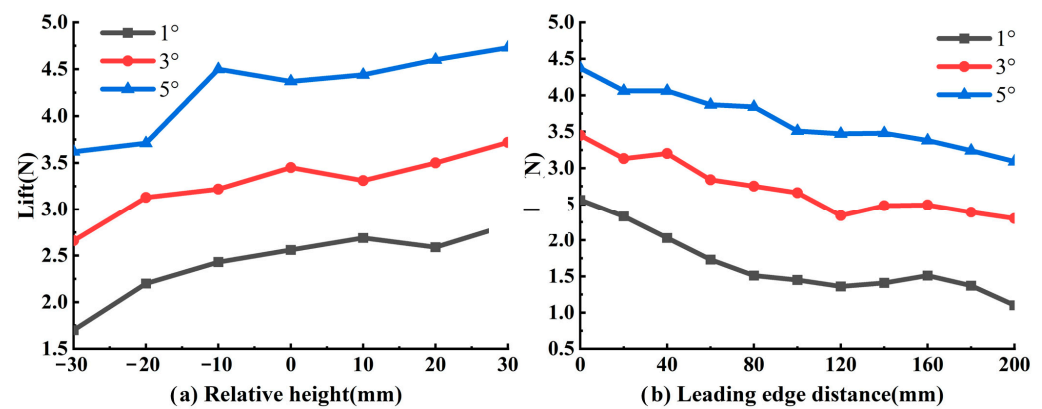


Figure 19. Comparison of test results at different angles of attack.

6. Conclusions

In this paper, we employ the actuator disk model to investigate the propeller slipstream effect on a distributed electric propulsion UAV. Simulations examining the impact of various relative heights, leading-edge distances, and rotational directions on the slipstream effect are performed. To enhance the UAV's lift coefficient during take-off and improve the lift-to-drag ratio during cruising, we employ a genetic algorithm to optimize the distributed propellers' layout. Simultaneously, we design a test platform to conduct a series of tests to validate our simulation results. The findings reveal the following:

- (1) The actuator disk can better replace the propeller for the numerical simulation of the slipstream flow field, which can meet the requirements of distributed propeller optimization design under the aerodynamic effect of the slipstream.
- (2) Following the optimization of the distributed propeller layout, the UAV wing's lift coefficient during the take-off phase has been significantly improved by 30.97%. The optimized aerodynamic layout proves to be more effective, and the lift/drag ratio of the wing is increased by 7.34%. This optimization is beneficial in boosting the drone's payload capacity and extending its cruise time.
- (3) The test results confirm that an increase in the relative height of the propellers indeed amplifies the lift of the wing. In theory, variations in the leading-edge distance exert minimal influence on the wing lift. However, in practice, the presence of surrounding stationary air consistently attenuates the airflow behind the disk. Thus, an increase in the leading-edge distance weakens the slipstream's lift effect on the wing.

Author Contributions: M.C. and K.L. designed research; M.C., K.L. and C.W. performed research; J.W., M.C. and Z.Q. analyzed and verified research; M.C. and J.W. wrote the paper. Our manuscript is original content and has not been submitted to other journals. All authors have read and agreed to the published version of the manuscript.

Funding: This research was funded by the Shenzhen Science and Technology Program (Grant No. JCYJ20200109142205924, GXWD20201231165807008).

Data Availability Statement: The supporting data of this study are available within the article.

Conflicts of Interest: The authors declare no conflict of interest.

References

1. Patterson, M.D.; German, B. Conceptual design of electric aircraft with distributed propellers: Multidisciplinary analysis needs and aerodynamic modeling development. In Proceedings of the 52nd Aerospace Sciences Meeting, National Harbor, MD, USA, 13–17 January 2014; p. 0534.
2. Moore, M.D. Misconceptions of electric aircraft and their emerging aviation markets. In Proceedings of the 52nd Aerospace Sciences Meeting, National Harbor, MD, USA, 13–17 January 2014; p. 0535.
3. Borer, N.K.; Patterson, M.D.; Viken, J.K.; Moore, M.D.; Bevirt, J.; Stoll, A.M.; Gibson, A.R. Design and performance of the NASA SCEPTOR distributed electric propulsion flight demonstrator. In Proceedings of the 16th AIAA Aviation Technology, Integration, and Operations Conference, Washington, DC, USA, 13–17 June 2016; p. 3920.
4. Patterson, M.D.; Derlaga, J.M.; Borer, N.K. High-lift propeller system configuration selection for NASA's SCEPTOR distributed electric propulsion flight demonstrator. In Proceedings of the 16th AIAA Aviation Technology, Integration, and Operations Conference, Washington, DC, USA, 13–17 June 2016; p. 3922.
5. Schnulo, S.L.; Chin, J.; Smith, A.; Paul-Dubois-Taine, A. Steady state thermal analyses of SCEPTOR X-57 wingtip propulsion. In Proceedings of the 17th AIAA Aviation Technology, Integration, and Operations Conference, Washington, DC, USA, 13–17 June 2016; p. 3783.
6. Christie, R.J.; Dubois, A.; Derlaga, J.M. *Cooling of Electric Motors Used for Propulsion on SCEPTOR*; AIAA: Reston, VA, USA, 2017.
7. Kelei, W.; Zhou, Z.; Zhongyun, F.; Jiahao, G. Aerodynamic design of tractor propeller for high-performance distributed electric propulsion aircraft. *Chin. J. Aeronaut.* **2021**, *34*, 20–35.
8. De Vries, R. Hybrid-Electric Aircraft with Over-the-Wing Distributed Propulsion: Aerodynamic Performance and Conceptual Design. Ph.D. Thesis, Delft University of Technology, Delft, The Netherlands, 2022.
9. Patterson, M.D.; Borer, N.K. Approach considerations in aircraft with high-lift propeller systems. In Proceedings of the 17th AIAA Aviation Technology, Integration, and Operations Conference, Washington, DC, USA, 13–17 June 2016; p. 3782.
10. Marcus, E.A.; de Vries, R.; Raju Kulkarni, A.; Veldhuis, L.L. Aerodynamic investigation of an over-the-wing propeller for distributed propulsion. In Proceedings of the 2018 AIAA Aerospace Sciences Meeting, Kissimmee, FL, USA, 8–12 January 2018; p. 2053.
11. de Vries, R.; van Arnhem, N.; Sinnige, T.; Vos, R.; Veldhuis, L.L. Aerodynamic interaction between propellers of a distributed-propulsion system in forward flight. *Aerosp. Sci. Technol.* **2021**, *118*, 107009. [[CrossRef](#)]
12. Sinnige, T.; van Arnhem, N.; Stokkermans, T.C.; Eitelberg, G.; Veldhuis, L.L. Wingtip-mounted propellers: Aerodynamic analysis of interaction effects and comparison with conventional layout. *J. Aircr.* **2019**, *56*, 295–312. [[CrossRef](#)]
13. Lei, Y.; Yang, W.-J.; Huang, Y.-Y. Aerodynamic performance of distributed electric propulsion with wing interaction. *J. Zhejiang Univ.-SCIENCE A* **2022**, *23*, 27–39. [[CrossRef](#)]
14. Zhang, X.; Zhang, W.; Weilin, L.; Zhang, X.; Tao, L. Experimental research on aero-propulsion coupling characteristics of a distributed electric propulsion aircraft. *Chin. J. Aeronaut.* **2023**, *36*, 201–212. [[CrossRef](#)]
15. Cheng, Z.; Yang, Y.; Ye, B. Parameterization investigation on distributed electric propulsion aircraft aerodynamic characteristics. *J. Phys. Conf. Ser.* **2018**, *2459*, 012092. [[CrossRef](#)]
16. Barakos, G.; Fitzgibbon, T.; Kusunov, A.; Kusunov, S.; Mikhailov, S. CFD simulation of helicopter rotor flow based on unsteady actuator disk model. *Chin. J. Aeronaut.* **2020**, *33*, 2313–2328. [[CrossRef](#)]
17. Stuermer, A. Unsteady CFD simulations of propeller installation effects. In Proceedings of the 42nd AIAA/ASME/SAE/ASEE Joint Propulsion Conference & Exhibit, Sacramento, CA, USA, 9–12 July 2006; p. 4969.
18. Stokkermans, T.C.; Van Arnhem, N.; Sinnige, T.; Veldhuis, L.L. Validation and comparison of RANS propeller modeling methods for tip-mounted applications. *AIAA J.* **2019**, *57*, 566–580. [[CrossRef](#)]
19. Stoll, A.M.; Bevirt, J.; Moore, M.D.; Fredericks, W.J.; Borer, N.K. Drag reduction through distributed electric propulsion. In Proceedings of the 14th AIAA Aviation Technology, Integration, and Operations Conference, Los Angeles, CA, USA, 12–14 August 2013; p. 2851.
20. Seo, Y.; Hong, Y.; Yee, K. Numerical investigation of wing-multiple propeller aerodynamic interaction using actuator disk method. *Int. J. Aeronaut. Space Sci.* **2022**, *23*, 805–822. [[CrossRef](#)]
21. Hassib, E.M.; El-Desouky, A.I.; El-Kenawy, E.-S.M.; El-Ghamrawy, S.M. An imbalanced big data mining framework for improving optimization algorithms performance. *IEEE Access* **2019**, *7*, 170774–170795. [[CrossRef](#)]
22. El-kenawy, E.-S.M.; Ibrahim, A.; Bailek, N.; Bouchouicha, K.; Hassan, M.A.; Jamei, M.; Al-Ansari, N. Sunshine duration measurements and predictions in Saharan Algeria region: An improved ensemble learning approach. *Theor. Appl. Climatol.* **2022**, *147*, 1015–1031. [[CrossRef](#)]
23. Takieldean, A.E.; El-kenawy, E.-S.M.; Hadwan, M.; Zaki, R.M. Dipper throated optimization algorithm for unconstrained function and feature selection. *Comput. Mater. Contin.* **2022**, *72*, 1465–1481. [[CrossRef](#)]
24. Abdelhamid, A.A.; El-Kenawy, E.-S.M.; Alotaibi, B.; Amer, G.M.; Abdelkader, M.Y.; Ibrahim, A.; Eid, M.M. Robust speech emotion recognition using CNN+ LSTM based on stochastic fractal search optimization algorithm. *IEEE Access* **2022**, *10*, 49265–49284. [[CrossRef](#)]
25. Xue, C.; Zhou, Z. Propeller-wing coupled aerodynamic design based on desired propeller slipstream. *Aerosp. Sci. Technol.* **2020**, *97*, 105556. [[CrossRef](#)]

26. Clarke, M.A.; Erhard, R.M.; Smart, J.T.; Alonso, J. Aerodynamic optimization of wing-mounted propeller configurations for distributed electric propulsion architectures. In Proceedings of the AIAA Aviation 2021 Forum, Virtual Event, 2–6 August 2021; p. 2471.
27. Le Chuiton, F. Actuator disc modelling for helicopter rotors. *Aerosp. Sci. Technol.* **2004**, *8*, 285–297. [[CrossRef](#)]
28. Li, B.; Lu, H.; Deng, S. Validation of an actuator disk model for numerical simulation of propeller. *Proc. Inst. Mech. Eng. Part G J. Aerosp. Eng.* **2015**, *229*, 1454–1463. [[CrossRef](#)]
29. Patterson, M.D. Conceptual Design of High-Lift Propeller Systems for Small Electric Aircraft. Ph.D. Thesis, Georgia Institute of Technology, Atlanta, GA, USA, 2016.
30. Deb, K.; Agrawal, S.; Pratap, A.; Meyarivan, T. A fast elitist non-dominated sorting genetic algorithm for multi-objective optimization: NSGA-II. In Proceedings of the Parallel Problem Solving from Nature PPSN VI: 6th International Conference, Paris, France, 18–20 September 2000; pp. 849–858.
31. Deb, K.; Goel, T. Controlled elitist non-dominated sorting genetic algorithms for better convergence. In Proceedings of the International Conference on Evolutionary Multi-Criterion Optimization, Leiden, The Netherlands, 20–24 March 2023; pp. 67–81.
32. Deb, K.; Pratap, A.; Agarwal, S.; Meyarivan, T. A fast and elitist multiobjective genetic algorithm: NSGA-II. *IEEE Trans. Evol. Comput.* **2002**, *6*, 182–197. [[CrossRef](#)]

Disclaimer/Publisher’s Note: The statements, opinions and data contained in all publications are solely those of the individual author(s) and contributor(s) and not of MDPI and/or the editor(s). MDPI and/or the editor(s) disclaim responsibility for any injury to people or property resulting from any ideas, methods, instructions or products referred to in the content.